sustainability

MDPI

Review

Simulation of Slag–Matte/Metal Equilibria for Complex and Low-Grade Raw Materials

Pekka Taskinen [1,*] and Katri Avarmaa [1,2]

[1] Department of Chemical and Metallurgical Engineering, School of Chemical Engineering, Aalto University, Kemistintie 1F, P.O. Box 16100, 00076 Espoo, Finland; kavarmaa@swin.edu.au
[2] Department of Mechanical and Product Design Engineering, Swinburne University of Technology, John Street, Melbourne 3122, Australia
* Correspondence: pekka.taskinen@aalto.fi

Abstract: The depleting and increasingly complex mineral resources bring challenges into the area of metal production, bringing new boundary conditions to the smelting and refining processes. Thermodynamics of phases and equilibria are the key to the analysis of pyrometallurgical processes, enabling descriptions of their limiting boundary conditions. The raw material basis of non-ferrous metals needs an effective control of iron oxide fluxing due to the challenging fact that the targeted metal values of, e.g., copper, nickel, lead, and tin will exist as minority components in the smelter feeds compared to iron sulphides, gangue, and many harmful elements. This means more complex slag compositions and the amount of produced slag being several times that of the metal production. This feature severely impacts the heat balance of the smelting vessels where autogenous operation without external fuels becomes more and more difficult to maintain.

Keywords: computational thermodynamics; non-ferrous metallurgy; phase equilibria; thermodynamics

Citation: Taskinen, P.; Avarmaa, K. Simulation of Slag–Matte/Metal Equilibria for Complex and Low-Grade Raw Materials. *Sustainability* **2021**, *13*, 12826. https://doi.org/10.3390/su132212826

Academic Editors: Peng Li and Marc A. Rosen

Received: 30 September 2021
Accepted: 17 November 2021
Published: 19 November 2021

1. Introduction

The primary raw materials of metals are important sources of many small metals, but their recovery is not feasible in current technologies. They include, e.g., cobalt and platinum group metals in nickel sulphides and antimony, selenium, and tellurium in copper sulphides [1,2]. WEEE (waste electric and electronic equipment) and other secondary sources of non-ferrous metals having short lifetime will become increasingly important sources of raw materials in the future to satisfy the growing demand of metals [3,4]. Their processing and separation from the materials streams into pure metals in the present smelting and refining technologies with high resource efficiency [5] and recovery rates of >90% will be one of the major industrial challenges of the upcoming decades [6–9].

Compared with the traditional copper secondaries, A and B type 'pure' copper scrap [10,11], the various fractions and types of WEEE as well as battery scrap introduced in the primary copper and nickel smelting and refining circuits bring new elements not familiar to, e.g., sulphide mineral raw materials. For their recovery, a large amount of fundamental research is needed for process optimisation purposes and for enabling their full recoveries [12,13].

Typically, high-conductivity copper for electric and thermal engineering purposes has been manufactured through the primary smelting–fire refining–electrolytic refining route, e.g., [14]. This processing chain is well tuned for maximising the recoveries of copper and its accompanying trace elements, such as the precious metals [15]. Now, WEEE will introduce increasing amounts of precious metals [16], but also, e.g., platinum group metals and various components of lead-free soldering alloys, such as tin [17–19], in the copper processing chain. Their distributions in the matte smelting of copper and nickel, copper converting, and electrolytic refining steps in main and side streams of metals, as well as in the black-copper smelting circuits, were still few years ago largely unknown [17,19–21].

Computational thermodynamics is the only practical tool for approaching large industrial systems with several components, tens of optional solution phases, and hundreds of possible solid substances [22]. It allows us to select the existing variables of the process in a consistent and solid way for exploring the conditions available for processing [23]. By this way, we can finetune the process optimisation efforts and maximise the resource efficiency of the available and forthcoming technologies [24].

This paper introduces the use of constrained phase equilibria of multi-component industrial systems in the process analysis where the boundary conditions are derived in a straightforward manner from the industrial reactors and their characteristic features. The present content of the used data source is introduced. The case studies use well-defined topics as examples for the copper and nickel smelting and refining industries, representing typical large heterogeneous systems and future challenges in the field.

2. Thermodynamic Databases

Several thermodynamic solvers include databases for equilibrium calculations [25]. In this paper, the extensive and internally fully consistent oxide database MTOX (vers. 8.1) was used with the MTDATA software package. The database has been under development since 1989 [26] under guidance of industrial partners. Today, it contains several extensive subsets of oxide and sulphide systems common in the minerals, metals, and inorganic chemical industries (see Figures 1 and A1, Figures A2 and A3 in Appendix A). The used solution models have been described elsewhere in detail [27]. In MTOX, only systems with 3rd and higher order assessments according to the Calphad method and its principles are included in the phase descriptions and no additive ternaries without e.g., ternary compounds, are presented as "early approximations".

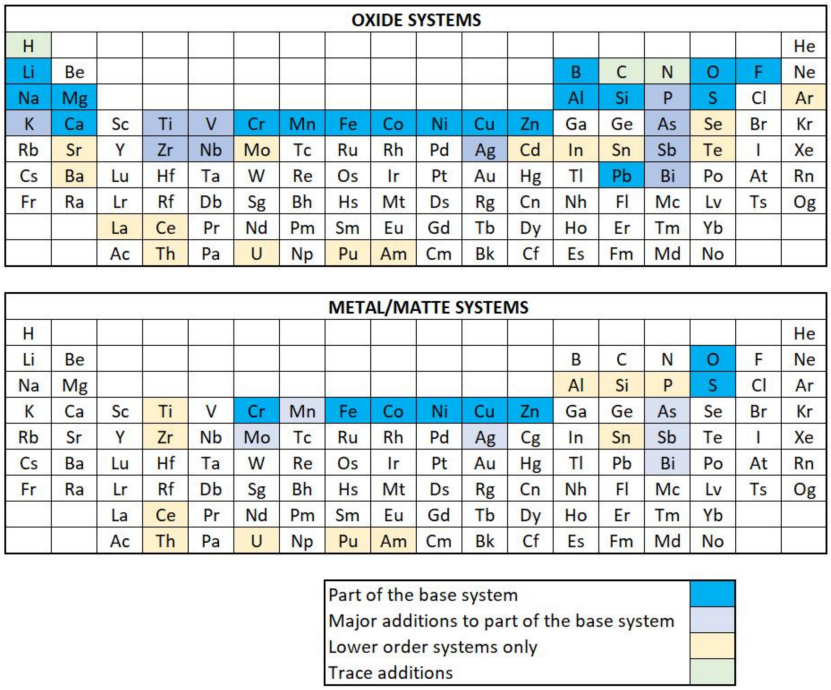

Figure 1. Coverage of the MTOX database (vers. 9.1) in oxide and metal alloy/matte systems [28].

3. Smelting and Refining Basics

This section provides a concise and precise description of the experimental results, their interpretation, and the experimental conclusions that were drawn.

3.1. Refining Equilibria in Secondary Copper Smelting

The driving force of removing alloying elements from copper is the oxygen activity or partial pressure according to the generic reaction:

$$[Me]_{Cu} + n^{1}/_{2}\, O_2(g) = (MeO_n) \quad (1)$$

where [] refers to the alloy, and () to the slag. The higher oxygen activity, the lower the concentration of Me in copper will be. For advancing reaction (1), the underlying crude copper dissolves oxygen and the dissolved oxygen in liquid copper is present as atomic oxygen:

$$^{1}/_{2}O_2(g) = [O]_{Cu} \quad (2)$$

Thus, copper–oxygen phase diagram generates another boundary condition for the system in addition to reaction (1) and its available oxygen partial pressure window in the refining. That fundamental constraint is visualised in Figure 2 at temperatures below the critical point of the Cu–O system at about 1350 °C [29,30], where selected oxygen iso-partial pressure contours at $p(O_2) = 10^{-3.5}$ to $10^{-7.0}$ atm have been plotted.

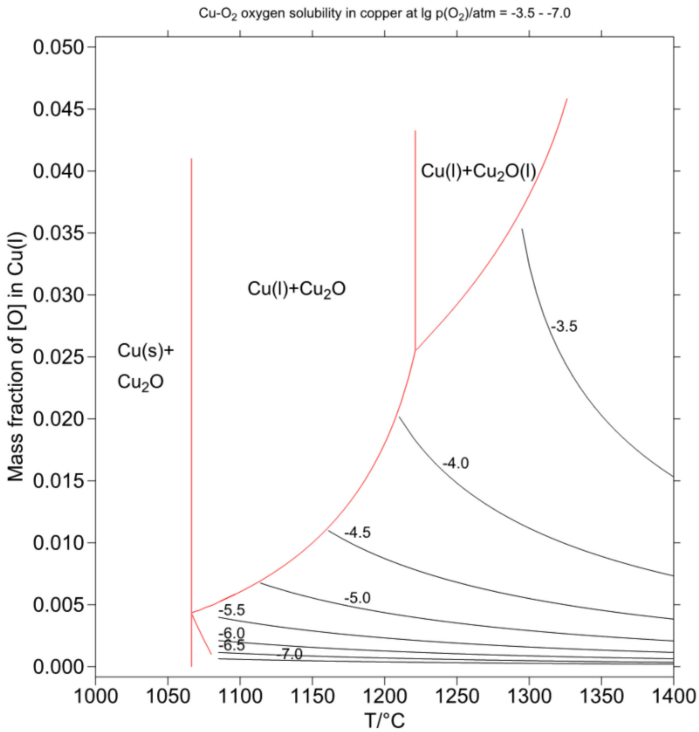

Figure 2. Solubility of oxygen in pure copper at constant oxygen partial pressures from 10^{-7} to $10^{-3.5}$ atm (solid lines). Calculated oxygen saturation boundary of the Cu–O system has been plotted with dashed line; MTDATA solver with MTOX database (vers. 8.1) [26].

3.2. Thermodynamics of Trace Elements in Smelting

All impurities and trace elements dissolve in the slags as oxidic species and therefore their chemistries are linked with the corresponding oxidation reactions and formation of the predominant cationic or anionic species in the slag, as with reaction (1) for cationic dissolution. The commonly used thermodynamic factor used for describing the behaviour of trace elements' behaviour in smelting and refining, the distribution coefficient of an element between two phases f1 and f2, $L^{f1/f2}(Me) = [\%Me]_{f1}/(\%Me)_{f2}$, is easily derived from Equation (1). This useful scale-independent factor, which in isothermal conditions can be written in logarithmic form as

$$\log L^{Cu/s}(Me) = C - n/2 \cdot \log p(O_2), \quad (3)$$

which has been recently measured for several 'technology metals' (Me = Co, Ni, Ga, In, and Sn) in various copper-making process environments, including matte smelting, copper matte converting, black copper smelting, and slag cleaning [16,17,31–33]. Selected trace elements have also been included in commercial and non-commercial solution databases for estimations of distributions in smelting [26,34,35].

4. Case Studies

4.1. Case 1: Copper Fire-Refining and Metal Distributions

In copper fire-refining, the equilibria (1) and (2) are utilised for transporting the impurities from crude copper. Reaction (1) clearly shows the impact of increasing oxygen activity in the process and lowering the activity coefficients of metal oxides in the refining slag.

The selection of refining slag suitable for effectively dissolving the oxidised trace elements is trickier in secondary smelting than in the primary smelting because the optimum point depends on the total fraction of impurities in the feed material. In this respect, a high-grade scrap provides more freedom for the fluxing chemistry due to small slag volume needed and the absence of, e.g., iron in the feed. As for thermodynamic features of reaction (1), the standard Gibbs energies of the oxides, a low refining temperature is favourable in the process for removing/oxidising the impurities.

The ultimate state or coverage of the thermodynamic databases for refining purposes is when we can calculate the equilibrium distributions of all elements between crude copper and potential slags. This, however, requires accurate experimentation of the alloy–slag equilibria for their modelling and optimisation of the thermodynamic properties which today is the case for some impurity elements typical to copper scrap only. Examples are arsenic, cobalt, iron, lead, nickel, and zinc within the coverage of the MTOX database [26].

In Figure 3, the boundary condition, constant oxygen partial pressure of $p(O_2)$ = 60 Pa (6×10^{-4} atm), controlled the behaviour of the distribution coefficient defined as $L^{Cu/s}$ (Ni) $\equiv$ [wt % Ni]$_{Cu}$/(wt % Ni)$_{slag}$. It regulated oxygen concentration of the Cu–O alloy in the homogeneous region, as indicated in Figure 1 with a red line. The lowest temperature of the diagram was limited by the stability of solid magnetite, which in this case precipitated from the slag at 1239 °C, dissolving significant fractions of nickel (5–10 wt %) in it as a (Fe, Ni) Fe_2O_4 solid solution at high oxygen partial pressures, around $p(O_2) = 10^{-4--5}$ atm [36,37].

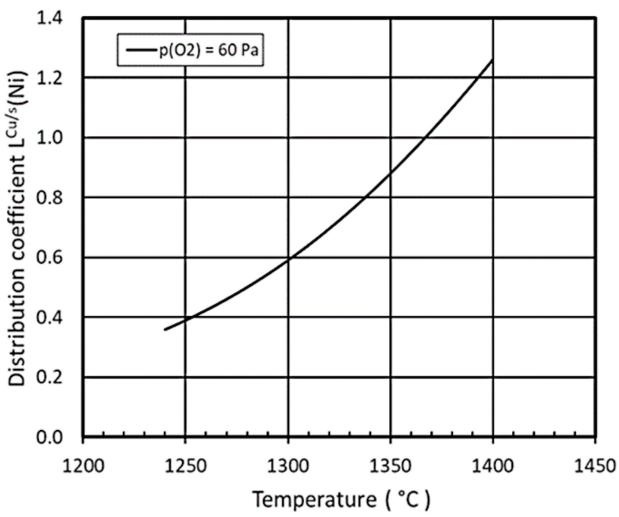

Figure 3. Calculated distribution coefficient of nickel between copper and a lime-bearing, low-silica iron silicate slag at $p(O_2)$ = 60 Pa ($\approx 6 \times 10^{-4}$ atm) and constant (wt % SiO_2) = 25 and (wt % CaO) = 2 as a function of temperature; MTDATA and MTOX database (vers. 8.1).

4.2. Case 2: The Assay of Silica Sand in Matte Smelting—Boundary Conditions in the Copper Smelting

In primary copper smelting, the general boundary conditions depend on the used technology and thus the operational parameters used in each stage of the processing. In the bath smelting processes, the maximum SO_2 partial pressure is fixed by the oxygen enrichment of the blow [38], whereas in the suspension smelting technologies, the physically separate oxidation and matte formation stages lead to the boundary condition $p(SO_2) \approx 1$ atm in the matte–slag interface during smelting [39].

All industrial copper (matte) smelting slags are based on fluxing solid iron oxides with silica. The forming molten iron silicate slag is able to effectively digest most gangue minerals (e.g., Al_2O_3, CaO, and K_2O) present in copper and nickel sulphide concentrates, with the significant exception of magnesia (MgO). The liquidus surface with isotherms of the ternary system FeO–Fe_2O_3–SiO_2 at 1150–1400 °C is shown in Figure 4. The yellow line shows 1250 °C isotherm and green 1350 °C isotherm. The oxygen activity of the slag or the partial pressure of O_2 (g) varies from iron saturation to pure oxygen from left to right, depending on temperature. Thus, the selected fluxing parameter, either target SiO_2 concentration or Fe/SiO_2 ratio of the slag, together with the prevailing oxygen partial pressure in furnace or converter matte, will define the operational point of the slag composition, i.e., its dissolved magnetite (or $FeO_{1.5}$) concentration.

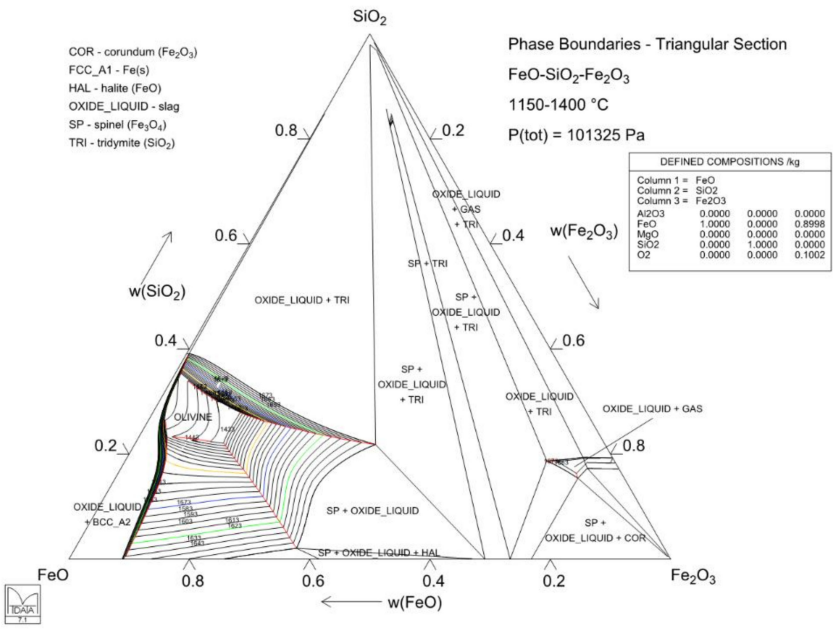

Figure 4. Calculated liquidus isotherm diagram of pure fayalite slags on FeO–SiO_2–Fe_2O_3 Gibbs triangle showing the phase relations at 1400 °C in P(tot) = 1 atm; the 1250 and 1350 °C isotherms are in colour.

Relatively small concentrations of 5–10 wt % gangue oxides significantly modified the liquid phase domain and affected the phase boundaries as well as the locations of the primary phase fields. Some examples are shown in Figure 5, where the impacts of 2.5 and 5 wt % of Al_2O_3 and K_2O, typical to natural sand, at 1300 °C on the fully liquid slag are demonstrated.

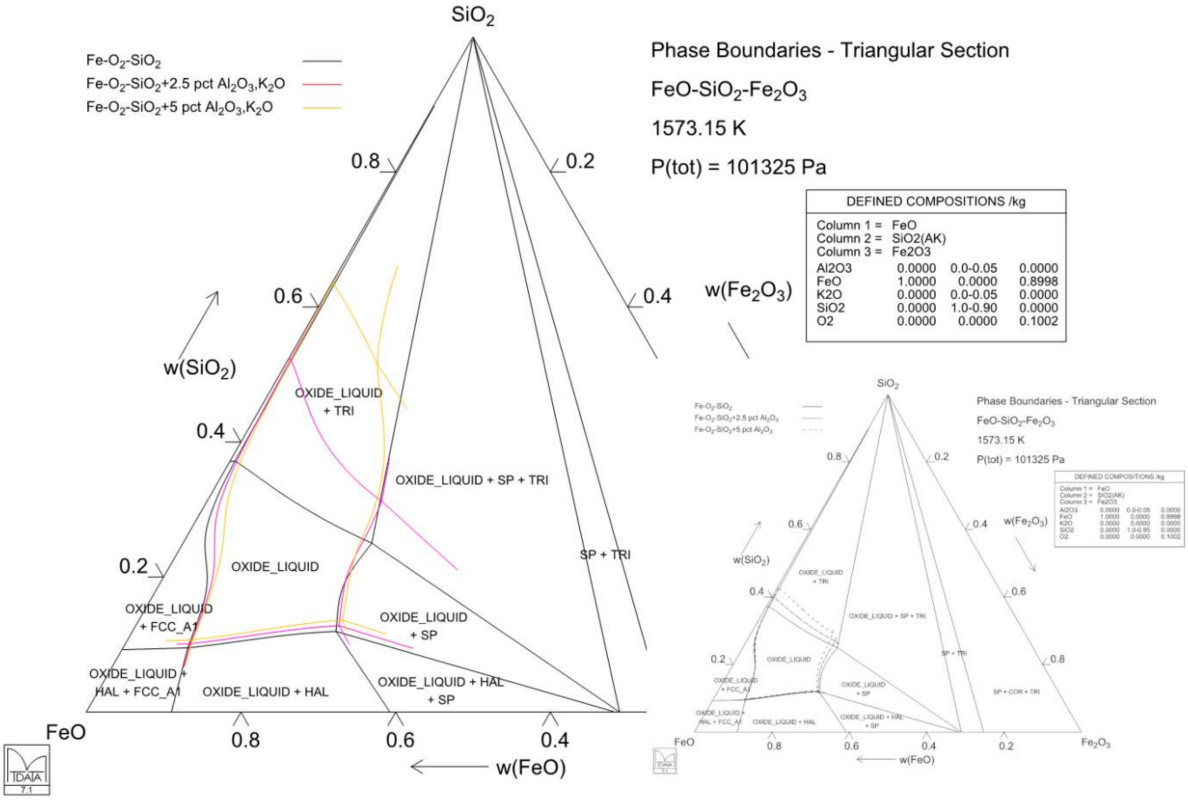

Figure 5. Calculated isothermal section of the system FeO–Fe_2O_3–SiO_2 at 1300 °C with small fractions (2.5 wt %) and (5 wt %) of alumina (Al_2O_3) and potassia (K_2O) introduced in the system in the silica flux (natural sand); the insert shows the phase relations without K_2O, i.e., the effect of alumina on the liquid slag domain.

The quality of flux in copper and nickel smelters varies from one location to another, depending on the available raw materials. Some smelters use quartzite mineral (essentially pure SiO_2) as flux, and in many cases riverbed or beach sands are used. Their typical minority minerals are alkali silicates, such as potassium feldspar ($KAlSi_3O_8$ as stoichiometric formula), containing 16.9 wt % K_2O and 18.3 wt % Al_2O_3. Because alkali oxides are well-known fluxes for silicates and alumina modifies the stability of spinel phases effectively, small fractions of feldspar have a strong effect on the molten phase domain of iron silicate slags.

Figure 5 shows a comparison of pure silica fluxing with natural sands where silica had fixed concentrations 2.5 and 2.5 wt % K_2O and Al_2O_3 (red line) as well as 5 and 5 wt % (green line), respectively. The black line of the ternary FeO–Fe_2O_3–SiO_2 system describes the phase boundaries in the alumina and potassia-free iron oxide–silica system. This comparison nicely demonstrates how the fraction of silica flux added in the smelting system influences the locations of silica and magnetite ('spinel') primary phase fields. Note that the diagrams with alumina and potassia extend to 95 and 90 wt % SiO_2 only in the top corner of the diagram.

The powerful influence of K_2O on the solubility of silica in the iron silicate slags and also on the melting point of the slag is shown in Figure 5. At 1300 °C, the silica primary phase field extended almost 25 wt % SiO_2 in reducing conditions, i.e., close to the FeO–SiO_2 sub-binary of the system, from the K_2O and Al_2O_3 free silica primary field boundary. The effect of alumina alone is depicted in the insert on the right-hand side.

4.3. Case 3: Solubility of Magnesia in Iron Silicate Slags—Slag Modification

The major industrial challenge faced by many smelters globally in the primary nickel matte smelting is MgO-rich gangue of nickel concentrates which may be solved either by a high smelting temperature or by slag modification with suitable flux additions, shifting the

olivine saturation boundary to higher concentrations of MgO. High-MgO gangue nickel concentrates can also be smelted by the new DON technology where the slag amount is extended by oxidising the feed mixture and its sulphidic iron in essence completely into the furnace slag [40].

The basic feature of the serious problem is illustrated in Figure 6, wherein the impact of MgO on the homogeneous liquid phase domain of iron silicate slags is illustrated when it was increased stepwise from 0 to 7.5 wt % at 1350 °C.

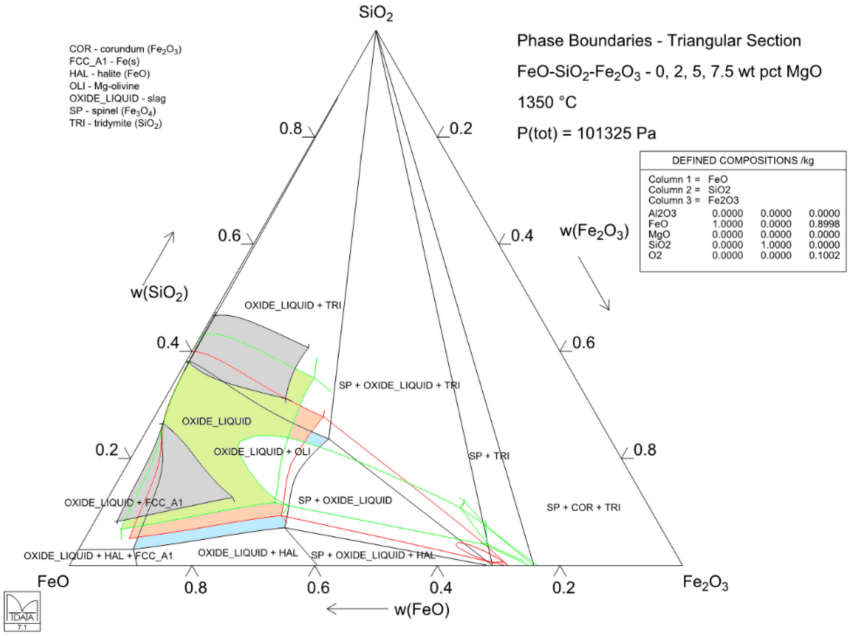

Figure 6. Deformation of the molten slag domain when MgO concentration increased from 0 to 7.5 wt % at 1350 °C: at the highest MgO addition of 7.5 wt %, the wide molten slag range split into two, generating a low-silica slag and high-silica slag; it was divided by solid olivine ($(Fe,Mg,Ni)_2SiO_4$) saturation 'belt', wherein the smelting operation was impossible due to high viscosity and slow slag tapping, limiting the production rate of the furnace.

The solubility limit of MgO was met already after 5 wt % (green phase domain in Figure 6) when solid olivine (in this system, a wide solid solution phase with formula ($(Co,Fe,Mg,Ni)_2SiO_4$) was stabilised and started to penetrate the liquid slag domain, splitting it into high-silica and low-silica slags. At 7.5 wt % MgO, the slag was fully divided into two molten domains, as shown by the grey phase boundaries in Figure 6. Thus, it limited the silica concentrations or Fe/SiO_2 ratios applicable in industrial conditions for fluxing the iron oxides formed in the smelting. The olivine saturation domain also showed increased viscosity due to solid particles floating in the slag and slowed down slag tapping.

Temperature dependence of the MgO solubility at fixed oxygen partial pressure (corresponding to a fixed matte grade) is shown in Figure 7. The isotherms 1300, 1350, and 1400 °C are highlighted in colour (green, orange, and blue, respectively) in Figure 7. Red contours indicate univariant lines with two solid phases stable at the same time with the liquid oxide, and the phase descriptions are presented on the left-hand side.

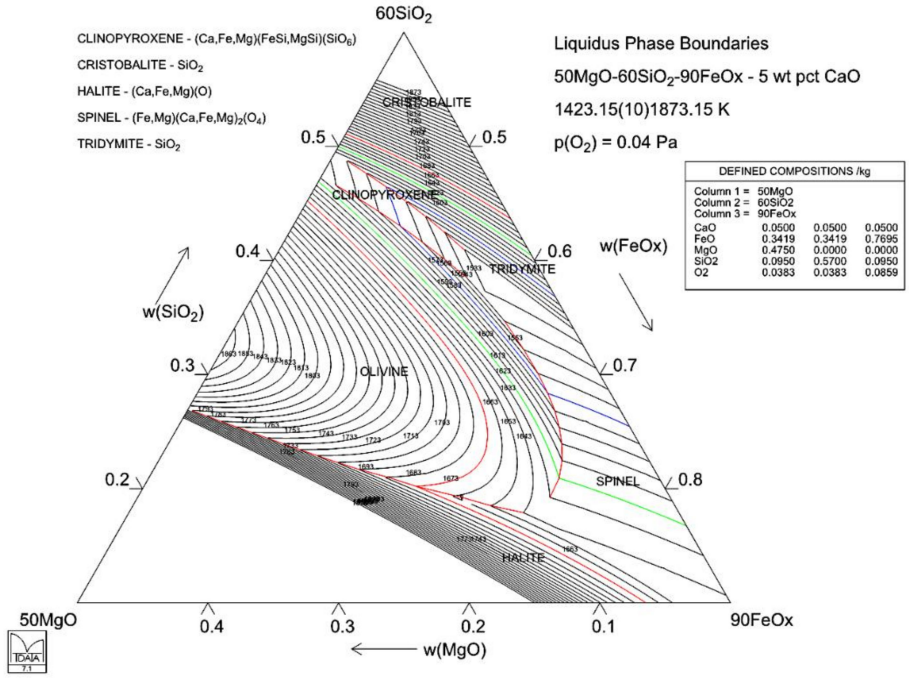

Figure 7. Liquidus isotherm plot of a part of the constrained system CaO–FeO–MgO–Fe_2O_3–SiO_2 in the temperature range of 1150–1400 °C, constant concentration of CaO = 5 wt % and at fixed oxygen partial pressure of $p(O_2)$ = 0.04 Pa (4×10^{-7} atm); MTDATA software with MTOX database.

Figure 7 indicates how the various primary phase fields (halite, spinel, olivine, clinopyroxene, and silica at industrially relevant temperatures and silica concentrations) behaved as a function of slag composition and the process temperature.

4.4. Case 4: Chemistry of Slag Cooling in Ladles

For improved metal recovery, copper slags are cooled slowly in large ladles prior to crushing and grinding for froth flotation. This technology was invented in the late 1960s in order to replace the direct cooling practices on slag heaps [41]. The primary target of the ladle cooling was the growing of particle size in the entrained matte, thus allowing for a more efficient settling of matte droplets during a typically 1–2 day cooling cycle. The technique allows for a more careful recovery of copper from the smelting and in some cases also matte converting slags [42].

In copper matte smelting slags, the chemically dissolved copper is less than 1 wt % (Cu). The equilibrium speciation at typical copper smelting temperatures and matte grades of 65 wt % [Cu] is predominantly as monovalent oxide species (Cu_2O or $CuO_{0.5}$) [2,43]. Industrial copper smelting slags typically contain 1.5–2.5 wt % copper depending on tapping practices and stability of the smelting operation [44]. The ladle cooling technology not only affect the mechanical dispersion of matte but also allows growth of the sub-micron metallic copper nuclei (<1 μm) formed in slag solidification close to its solidus temperature as

$$(CuO_{0.5}) + (FeO) = Cu^{\circ} + (FeO_{1.5}) \quad (4)$$

This process is demonstrated in the slag–matte cooling equilibria in Figure 8. It also shows the reduction of sulphur and thus matte solubility in the slag when it cools down. The resulting very fine metal dispersion can be found in solidified microstructures of the industrial copper slags where very fine copper particles are embedded in the glassy intermediate phase, originally representing the molten residual slag.

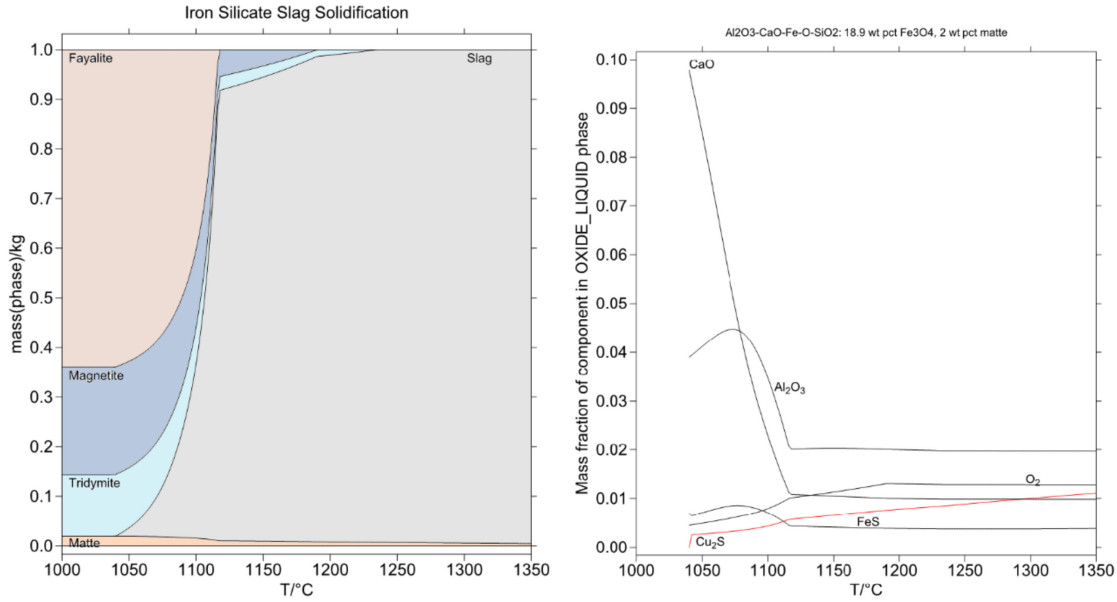

(**a**) (**b**)

Figure 8. Composition of liquid fraction of an iron silicate slag (2 wt % Al_2O_3–1 wt % CaO–Fe–SiO_2–O_2) in equilibrium with a copper matte during cooling from 1350 to 1050 °C. Note the sudden decrease of copper (Cu_2S) solubility at the final solidification (no interactions with the gas phase during cooling); (**a**) Phase fractions during slag solidification; (**b**) Minority components in the liquid slag.

The strong stability of ferric oxide during slag solidification, with reference to cuprous oxide, and formation of the tiny magnetite ('spinel') crystallites also generates the driving force for depleting impurity elements dissolved in the molten silicate slag. This is demonstrated in Figure 9, where the equilibrium phase distributions of antimony, arsenic, and lead between the stable phases are depicted. The used computational temperature window extended from typical copper matte smelting at 1250–1350 °C down to 900 °C in order to reveal distribution behaviours of the trace elements below the melting point of pure copper (1358 K) and the copper–oxygen eutectic temperature (1045 °C; [45,46]). In the computational system, 2 wt % of copper–iron matte was defined in the initial slag mixture to mimic the mechanical entrainment of matte. The concentrations of the impurities were 1 wt % each of the total amount of the dispersed matte. The process follows, therefore, a chemical reaction sequence e.g., for lead, which in iron silicate slags exists predominantly as a monovalent oxide species [47], shown by the following reaction:

$$(PbO) + 2\,(FeO) = [Pb] + 2(FeO_{1.5}) \quad (5)$$

where [Pb] denotes lead dissolving in the matte–metal phases on either side of the liquid state miscibility gap. It enriches the remaining matte droplets and copper nuclei with impurities. Therefore, this process generates low melting point copper alloys in the matte–metal droplets and circulates impurities back to the smelting step.

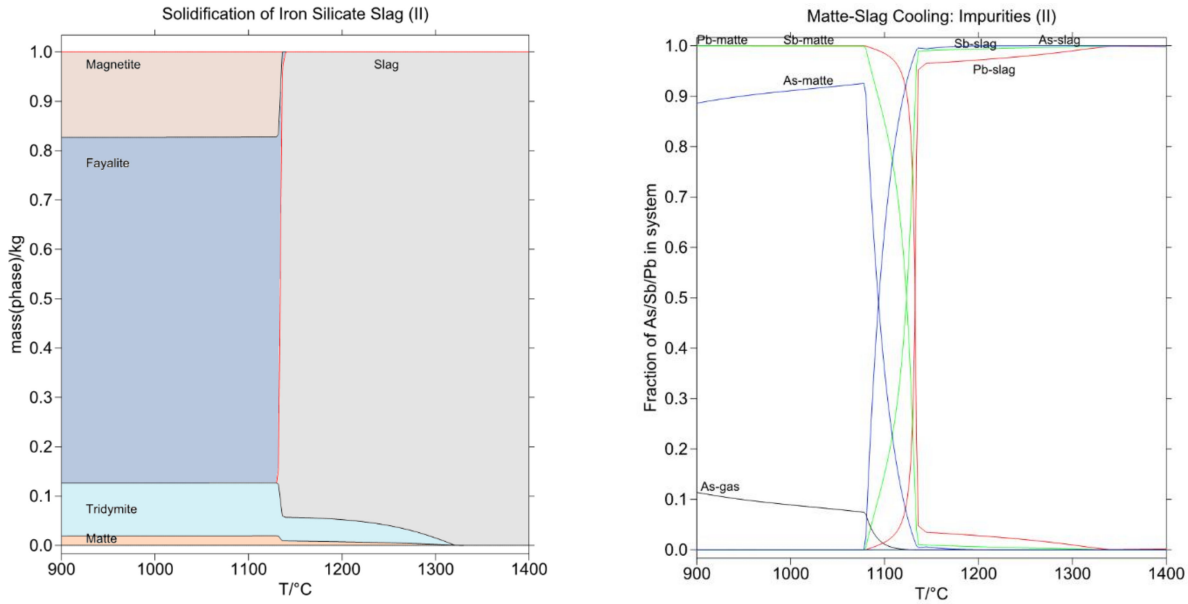

(**a**) (**b**)

Figure 9. The distribution equilibria of antimony, arsenic, and lead between the stable phases during slag–matte cooling in the copper matte–FeO–Fe_2O_3–SiO_2 slag system with gas phase. Their deportment from slag to matte/metal was almost total during final slag solidification and some 30–50 °C below it (see Figure 8); (**a**) Phase fractions during slag (II) solidification; (**b**) Distributions of As, Pb, and Sb during solidification.

The impact of slag solidification on the weak oxide-forming impurity elements was found to be substantial. The trace elements indicated predominantly deported in the slag at high temperatures but were reduced to the matte–alloy phase when the slag was solidifying. This also cleaned the iron silicate slag from the trace elements dissolved in it at the smelting temperature. Thus, the downside was that the fraction recovered from the slag after controlled cooling, milling, and froth flotation with a high yield of copper and its impurities (As, Sb, and Pb) was fed back to the smelting cycle where it constantly increased the impurity amounts together with the flue dust circulation from the off-gas train.

In Figure 9, the gas phase was defined in the system for demonstrating the vaporisation tendency of the trace elements studied. Only a significant fraction of arsenic existed in the gas (Ar) after it was transferred to the sulphide matte during slag solidification. This may be a hygienic problem in the ladle cooling sites, even if the free surface exposed to atmosphere in ladle is small.

5. Conclusions

Thermodynamic properties of phases and phase equilibria are the key to the analysis of pyrometallurgical processes, and they enable us to describe the limiting boundary conditions of metallurgical systems in a solid straightforward way. In order to reach this aim, more reliable, internally consistent thermodynamic databases are needed, and many white gaps in the experimental data on industrially relevant oxide and sulphide systems must be filled with reliable and validated observations. This is equally valid for the main components of the slags, as well as for the minority and trace elements.

Minimisation of the slag/metal ratio in smelting and effective fluxing strategies are the major challenges of the non-ferrous smelting and refining industry in the future, which will be additionally tested by the massive use of secondaries required by the ethical use of natural resources and the circular economy. Behind these requirements also is the need to secure resource efficiency of metal extraction and availability of the engineering and high-tech metals in the future.

This is a specific need where computational thermodynamics helps us beyond the hard copies of three-component and constrained four-component phase diagrams in various compilations, once reliable databases are available.

The smelting of lean and complex raw materials is a sizable and complex issue where the metal value recoveries and elimination of harmful elements in a controlled way may involve contradictory requirements and boundary conditions. There, the use of phase equilibria of large chemical systems of industrial importance will be used effectively once the necessary and accurate fundamental property data of the phases are available.

Author Contributions: K.A., P.T., conceptualisation; P.T., writing—original draft preparation; K.A., writing—review and editing. All authors have read and agreed to the published version of the manuscript.

Funding: Katri Avarmaa is grateful for the Finnish Steel and Metals Producers Fund via Daniel Lindberg's research group grant (grant application number #1497).

Institutional Review Board Statement: Not applicable.

Informed Consent Statement: Not applicable.

Acknowledgments: The authors are indebted to Aalto University and Academy of Finland for providing the use of facilities of RAMI (RawMatTERS Finland Infrastructure) based at Aalto University, GTK, and VTT in Espoo in this study.

Conflicts of Interest: The authors declare no conflict of interest.

Appendix A. Fully Assessed Systems Included in MTOX Database, Vers. 9.1

CaO-Co-Cr-Cu-Fe-Ni-O-MgO-PbO-ZnO-Al_2O_3-SiO_2-S
Li_2O-Na_2O-CaO-Cr-Fe-**Mn**-O-MgO-Al_2O_3-**B_2O_3**-SiO_2, Cu-Fe-**Mo**-O
Li_2O-Na_2O-CaO-Fe-Mn-O-MgO-Al_2O_3-B_2O_3-SiO_2-**F** (including CaF_2, MgF_2, NaF, Na_3AlF_6, LiF)
Li_2O-Na_2O-CaO-MgO-Al_2O_3-SiO_2-**ZrO_2-V_2O_5**, CaO-B_2O_3-ZrO_2, MgO-B_2O_3-ZrO_2, B_2O_3-SiO_2-ZrO_2
B_2O_3-Na_2O-ZrO_2, B_2O_3-Al_2O_3-ZrO_2
Na_2O-**K_2O**-MgO-NiO-Al_2O_3-ZrO_2-V_2O_5-**SO_3**, K_2O-CaO-B_2O_3, K_2O-MgO-B_2O_3, Na_2O-K_2O-B_2O_3, K_2O-Fe-O-B_2O_3, K_2O-Al_2O_3-B_2O_3, K_2O-B_2O_3-SiO_2, K_2O-Na_2O-CaO-Cu-Fe-O-MgO-Al_2O_3-SiO_2-S
K_2O-CaO-Mn-O, K_2O-MgO-Mn-O, K_2O-Na_2O-Mn-O, K_2O-Na_2O-CaO-Fe-Ni-O-MgO-ZnO-Al_2O_3-SiO_2
Na_2O-Fe-O-ZrO_2, CaO-Fe-O-MgO-Al_2O_3-**V_2O_3**-SiO_2, V_2O_3-V_2O_5
Na_2O-CaO-MgO-Al_2O_3-SiO_2-ZrO_2-**P_2O_5**-V_2O_5, CaO-Fe-O-MgO-Al_2O_3-SiO_2-P_2O_5, Ni-O-P_2O_5, Fe-O-V_2O_5
CaO-Fe-**Ti**-Zr-O-MgO-Al_2O_3-SiO_2, Na_2O-K_2O-TiO_2, CaF_2-CaO-Ti-O, Na_2O-Ti-O-Al_2O_3, Na_2O-Ti-O-MgO
Na_2O-Ti-O-SiO_2, Na_2O-Ti-O-ZrO_2, **Sn**-Zn-O, **Am**-O, **Pu**-O
As-Cu-Fe-Ni-O-CaO-MgO-Al_2O_3-SiO_2-S, As-Cr-O, As-Ni-Pb-O, As-O-K_2O, As-O-Na_2O, As-Fe-Pb-O
As-**Bi**-Cu-O, As-Bi-Fe-O, As-Bi-Ni-O, As-Bi-Pb-O, Bi-Cu-Pb-O, Bi-Fe-Ni-O, Bi-Fe-Pb-O, Bi-Ni-Pb-O
Bi-Cu-Fe-O-CaO-MgO-Al_2O_3-SiO_2, Fe-**Nb**-O-Al_2O_3-SiO_2, Fe-O-MgO-Al_2O_3-TiO_2-Nb_2O_5, CaO-Nb_2O_5, Cr-O-Nb_2O_5
Ce-O, CaO-MgO-CeO_2, Fe-O-CeO_2, CaO-Al_2O_3-CeO_2, CaO-CeO_2-SiO_2, MgO-CeO_2-SiO_2, MgO-Al_2O_3-CeO_2, Al_2O_3-CeO_2-SiO_2
Ag-Pb-O, Ag-Cu-O-CaO, Ag-O-CaO-Al_2O_3, Ag-O-CaO-SiO_2, Ag-As-O-SiO_2, Ag-O-Al_2O_3-SiO_2, Ag-Cu-Fe-O, Ag-Fe-O-CaO, Ag-Fe-O-Al_2O_3
KNO_3-$NaNO_3$-$Ca(NO_3)_2$-$Mg(NO_3)_2$ (**NO_3^-** solubility in K_2O-Na_2O-CaO-Fe-O-MgO-Al_2O_3-SiO_2 liquids)

Figure A1. Oxides.

Co-Cu-Cr-Fe-Ni-Pb-Zn-O-**S**, Cu-Fe-**Mn**-S, Cu-Fe-Ni-Mn-S, Al-Fe-**Ti**-Si-**Zr**
Ag-Fe-S, **As**-Cu-Pb-S, As-Pb-O-S, **Sb**-O-S, **Bi**-Cu-S, Bi-Fe-S, Bi-Pb-S, **Mo**-S
As-Bi-Cu, As-Bi-Fe, Bi-Cu-Ni, Bi-Fe-Ni, Bi-Fe-Pb, Bi-Ni-Pb, Bi-Fe-S
As-Bi-Ni-S, As-Bi-Pb-S, Bi-Cu-Pb-S
Mo-Mn, Cu-Fe-Mo, Cr-Fe-Mo, Cr-Mn-Ni, Cr-Mo-Ni, Fe-Mo-Ni, Cu-Mo-S, Fe-Mn-Mo, Fe-Mo-O-S
Ag-As-Pb, Ag-O-S, Ag-Cu-S, **Am-Pu-U**, Pu-**Th**-U
Al binary systems with Ag, **Ce**, Cr, Cu, Mn, **P**, **Sn**
Si binary systems with Ce, Cr, Cu, Mn, Sn

Figure A2. Sulphides and metals.

Hydroxyl capacity of CaO-Fe-O-MgO-Al_2O_3-SiO_2, Na_2O-SiO_2, K_2O-SiO_2 oxide liquids
Sulphate capacity of Na_2O-CaO-Al_2O_3-SiO_2 oxide liquids
Carbonate solubility in CaF_2-K_2O-Na_2O-CaO-Fe-O-MgO-Al_2O_3-SiO_2-TiO_2 oxide liquids.
C and CN solubility in CaO-Al_2O_3-B_2O_3-SiO_2 oxide liquids

Figure A3. Trace elements in the liquid oxide solutions.

References

1. Moats, M.; Alagha, L.; Awuah-Offei, K. Towards resilient and sustainable supply of critical elements from the copper supply chain: A review. *J. Clean. Prod.* **2021**, *307*, 127207. [CrossRef]
2. Klaffenbach, E.; Mostaghel, S.; Guo, M.; Blanpain, B. Thermodynamic analysis of copper smelting, considering the impact of minor elements behavior on slag application options and Cu recovery. *J. Sust. Metall.* **2021**, *7*, 664–683. [CrossRef]
3. Ayres, R.U.; Talens Peiró, L. Materials efficiency: Rare and critical metals. *Phil. Trans. R. Soc. A* **2013**, *372A*, 20110563. [CrossRef] [PubMed]
4. Rhys, C.; Douglas, P.; Dowling, M.; Liversage, G.; Davies, M. Towards Increased Recovery of Critical Metals from WEEE-evaluation of CRMs at a component level and pre-processing methods for interface optimisation with recovery processes. *Res. Conserv. Recycl.* **2020**, *161*, 104923.
5. Alexander, C.; Johto, H.; Lindgren, M.; Pesonen, L.; Roine, A. Comparison of environmental performance of modern copper smelting technologies. *Clean. Environm. Syst.* **2021**, *3*, 100051. [CrossRef]
6. Cisternas, L.A.; Ordonez, J.I.; Jeldres, R.I.; Serna-Guerrero, R. Toward the Implementation of Circular Economy Strategies: An Overview of the Current Situation in Mineral Processing. *Miner. Process. Extr. Met. Rev.* **2021**, 1–23. [CrossRef]
7. Alvear Flores, G.; Risopatron, C.; Pease, J. Processing of Complex Materials in the Copper Industry: Challenges and Opportunities Ahead. *JOM* **2020**, *72*, 3447–3461. [CrossRef]
8. Nakamura, S.; Kondo, Y.; Nakajima, K.; Ohno, H.; Pauliuk, S. Quantifying Recycling and Losses of Cr and Ni in Steel Throughout Multiple Life Cycles Using MaTrace-Alloy. *Environ. Sci. Technol.* **2017**, *51*, 9469–9476. [CrossRef] [PubMed]
9. Ciacci, L.; Harper, E.M.; Nassar, N.T.; Reck, B.K.; Graedel, T.E. Metal Dissipation and Inefficient Recycling Intensify Climate Forcing. *Environ. Sci. Technol.* **2016**, *50*, 11394–11402. [CrossRef] [PubMed]
10. Copper Development Association Inc.: McLean, VA, USA. 2021. Available online: https://www.copper.org/environment/lifecycle/ukrecyc.html (accessed on 18 November 2021).
11. Muchova, L.; Eder, P.; Villanueva, A. *End-of-Waste Criteria for Copper and Copper Alloy Scrap*; Report EUR 24786 EN; JRC-IPTS: Luxembourg Publications Office of EU: Luxembourg, 2011; p. 118.
12. Hsu, E.; Barmak, K.; West, A.C.; Park, A.-H. Advancements in the treatment and processing of electronic waste with sustainability: A review of metal extraction and recovery technologies. *Green. Chem.* **2019**, *21*, 919–936. [CrossRef]
13. Shishin, D.; Shevschenko, M.; Jak, E. Experimental Study and Thermodynamic Calculations in the CaO-Cu_2O-FeO-Fe_2O_3-SiO_2 System and Application in Novel Copper-Based Processes. *J. Sustain. Metall.* **2020**, *7*, 300–311. [CrossRef]
14. Rötzer, N.; Schmidt, M. Historical, Current, and Future Energy Demand from Global Copper Production and its Impact on Climate Change. *Resources* **2020**, *9*, 44. [CrossRef]
15. Chen, M.; Avarmaa, K.; Klemettinen, L.; O'Brien, H.; Sukhomlinov, D.; Shi, J.; Taskinen, P.; Jokilaakso, A. Recovery of Precious Metals (Au, Ag, Pt, and Pd) from Urban Mining through Copper Smelting. *Metall. Mater. Trans. B* **2020**, *51B*, 1495–1508. [CrossRef]
16. Zhang, S.; Ding, Y.; Liu, B.; Chang, C. Supply and demand of some critical metals and present status of their recycling in WEEE. *Waste Manag.* **2017**, *63*, 113–127. [CrossRef] [PubMed]
17. Avarmaa, K.; Yliaho, S.; Taskinen, P. Recoveries of rare elements Ga, Ge, In and Sn from Waste Electric and Electronic Equipment through Secondary Copper Smelting. *Waste Manag.* **2018**, *71*, 400–410. [CrossRef] [PubMed]
18. Van Nielen, S.S.; Kleijn, R.; Sprecher, B.; Xicotencatl, B.M.; Tukker, A. Early-stage assessment of minor metal recyclability. *Res. Conserv. Recycl.* **2022**, *176*, 105881. [CrossRef]

19. Avarmaa, K.; Klemettinen, L.; O'Brien, H.; Taskinen, P. Urban mining of precious metals via oxidizing copper smelting. *Miner. Eng.* **2019**, *133*, 95–102. [CrossRef]
20. Shuva, M.A.H.; Rhamdhani, M.A.; Brooks, G.A.; Masood, S.; Reuter, M.A.; Firdaus, M. Analysis for Optimum Conditions for Recovery of Valuable Metals from E-waste Through Black Copper Smelting. In *Proceedings of the 8th International Symposium on High-Temperature Metallurgical Processing, San Diego, CA, USA, 26 February–2 March 2017*; Springer: Cham, Switzerland, 2017; pp. 419–427.
21. Reck, B.K.; Graedel, T.E. Challenges in Metal Recycling. *Science* **2012**, *337*, 690–695. [CrossRef]
22. Hack, K. *SGTE Casebook*, 2nd ed.; Taylor Francis Inc.: Boca Roca, FL, USA, 2008; p. 300.
23. Jak, E.; Hidayat, T.; Shishin, D.; Mehrjardi, A.F.; Chen, J.; Hayes, P. Experimental and modelling research in support of energy savings and improved productivity in non-ferrous metal production and recycling. In *Proceedings of the European Metallurgical Conference, EMC. Leipzig, Germany, 25–28 June 2017*; GDMB Verlag: Clausthal-Zellerfeld, Germany, 2017; pp. 231–250.
24. Reuter, M.A.; van Schaik, A. Resource Efficient Metal and Material Recycling. In *Rewas 2013*; Kvithyld, A., Meskers, C., Kirchain, G., Eds.; TMS: Warrendale, PA, USA; pp. 332–340.
25. Jung, I.-H. Overview of the applications of thermodynamic databases to steelmaking processes. *Calphad* **2010**, *34*, 332–362. [CrossRef]
26. Gisby, J.; Taskinen, P.; Pihlasalo, J.; Li, Z.; Tyrer, M.; Pearce, J.; Avarmaa, K.; Björklund, P.; Davies, H.; Korpi, M.; et al. MTDATA and the Prediction of Phase Equilibria in Oxide Systems: 30 years of Industrial Collaboration. *Metall. Mater. Trans. B* **2017**, *48B*, 91–98. [CrossRef]
27. Barry, T.; Dinsdale, A.T.; Gisby, J.A. Predictive Thermochemistry and Phase Equilibria of Slags. *JOM* **1993**, *45*, 32–38. [CrossRef]
28. *Ham 2020. HTOX Version 9.1—Release Notes*; Hampton Thermodynamics: Hampton, UK, 2020.
29. Taskinen, P. Thermodynamics of liquid copper-oxygen alloys at 1065–1450 °C. *Scand. J. Metall.* **1984**, *13*, 75–82.
30. Shishin, D.; Decterov, S. Critical assessment and thermodynamic modeling of the Cu-O and Cu-O-S systems. *Calphad* **2012**, *38*, 59–70. [CrossRef]
31. Avarmaa, K.; O'Brien, H.; Klemettinen, L.; Taskinen, P. Precious metal recoveries in secondary copper smelting with high-alumina slags. *J. Mater. Cycles Waste Manag.* **2020**, *22*, 642–655. [CrossRef]
32. Avarmaa, K.; Taskinen, P.; Klemettinen, L.; O'Brien, H.; Lindberg, D. Ni-Fe-Co Alloy—Magnesia-Iron-Silicate Slag Equilibria and the Behavior of Minor Elements Cu and P in Nickel Slag Cleaning. *J. Mater. Res. Technol.* **2021**, *15*, 719–730. [CrossRef]
33. Dańczak, A.; Klemettinen, L.; O'Brien, H.; Taskinen, P.; Lindberg, D.; Jokilaakso, A. Slag Chemistry and Behavior of Nickel and Tin in Black Copper Smelting with Alumina and Magnesia-containing Slags. *J. Sust. Metall.* **2021**, *7*, 1–14. [CrossRef]
34. Shishin, D.; Hayes, P.; Jak, E. Development and Applications of Thermodynamic Database in Copper Smelting. In *Proceedings of the Copper 2019 Conference, 2 Pyrometallurgy, Vancouver, VA, Canada, 18–21 August 2019*; CIM-MetSoc: Montreal, Canada, 2019; p. 12.
35. Sineva, S.; Shevchenko, M.; Shishin, D.; Hidayat, T.; Chen, J.; Hayes, P.C.; Jak, E. Phase equilibria and minor element distributions in complex copper/slag/matte systems. *JOM* **2020**, *72*, 3401–3409. [CrossRef]
36. Chen, M.; Avarmaa, K.; Taskinen, P.; Klemettinen, L.; Michallik, R.; O'Brien, H.; Jokilaakso, A. Handling trace elements in WEEE recycling through copper smelting-an experimental and thermodynamic study. *Miner. Eng.* **2021**, *173*, 107189. [CrossRef]
37. Klemettinen, L.; Avarmaa, K.; Taskinen, P. Slag Chemistry of High-alumina Iron Silicate Slags at 1300 °C in WEEE Smelting. *J. Sustain. Metall.* **2017**, *3*, 772–781. [CrossRef]
38. Kapusta, J.; Larouche, F.; Palumbo, E. Adoption of high oxygen bottom blowing in copper matte smelting: Why it is taking so long? In *Proceedings of the COM2015 The Conference of Metallurgists, Toronto, ON, Canada, 23–26 August 2015*; CIM-MetSoc: Montreal, Canada, 2015; pp. 1–25.
39. Taskinen, P. Direct-to-blister smelting of copper concentrates: The slag fluxing chemistry. *Miner. Process. Extr. Metall.* **2011**, *120*, 240–246. [CrossRef]
40. Johto, H.; Latostenmaa, P.; Peuraniemi, E.; Osara, K. Review of Boliden Harjavalta Nickel Smelter. In *Extraction 2018*; Davis, B., Moats, M., Wang, S., Eds.; TMS: Warrendale, PA, USA, 2018; pp. 81–87.
41. Submaranian, K.N.; Themelis, N.J. Copper recovery by flotation. *JOM* **1972**, *24*, 33–38. [CrossRef]
42. Jalkanen, H.; Vehviläinen, J.; Poijärvi, J. Copper in solidified copper smelter slags. *Scand. J. Metall.* **2003**, *32*, 65–70. [CrossRef]
43. Kim, H.G.; Sohn, H.Y. Minor-Element Behavior and Iron Partition during the Cleaning of Copper Converter Slag under Reducing Conditions. *Can. Metall. Q* **1997**, *36*, 31–37. [CrossRef]
44. Sridhar, R.; Toguri, J.; Simeonov, S. Copper losses and thermodynamic considerations in copper smelting. *Metall. Mater. Trans. B* **1997**, *28B*, 191–200. [CrossRef]
45. Schramm, L.; Behr, G.; Löser, W.; Wetzig, K. Thermodynamic reassessment of the Cu-O phase diagram. *J. Phase Equilibria Diffus.* **2005**, *26*, 605–612. [CrossRef]
46. Hallstedt, B.; Risold, D.; Gauckler, L.J. Thermodynamics Assessment of the Copper-Oxygen System. *J. Phase Equil.* **1994**, *15*, 483–499. [CrossRef]
47. Sineva, S.; Shishin, D.; Starykh, R.; Hayes, P.C.; Jak, E. Equilibrium Distributions of Pb, Bi, and Ag between Fayalite Slag and Copper-Rich Metal, Calcium Ferrite Slag and Copper-Rich Metal. Thermodynamic Assessment and Experimental Study at 1250 °C. *J. Sust. Metall.* **2021**, *7*, 569–582. [CrossRef]